Homogeneous CuGaSe_2 growth by the CuPRO process with In-Situ AgBr treatment

Elizabeth Palmiotti, Polyxeni Tsoulka, Deewakar Poudel, Sylvain Marsillac, Nicolas Barreau, Angus Rockett, Thomas Lepetit

Homogeneous $CuGaSe_2$ Growth by the CuPRO Process with In-Situ AgBr Treatment

Elizabeth Palmiotti[a], Polyxeni Tsoulka[b], Deewakar Poudel[c], Sylvain Marsillac[c], Nicolas Barreau[b], Angus Rockett[a], Thomas Lepetit[b]

[a] Colorado School of Mines, Department of Metallurgical and Materials Engineering, Golden, CO, 80401, U.S.A.

[b] Université de Nantes, CNRS, Institut des Matériaux Jean Rouxel, IMN, F-44000, Nantes, 44300, France

[c] Old Dominion University, Virginia Institute of Photovoltaics, Norfolk, VA, 23606 U.S.A.

Abstract

Homogeneous $CuGaSe_2$ thin film growth is limited by slow kinetics of formation. A modified growth process was previously developed to address this issue but requires two separate long, high temperature anneals. Here, we demonstrate that a short AgBr treatment can replace this modified growth process. The AgBr works as a transport agent to catalyze $CuGaSe_2$ formation and atomic mobility. This treatment results in large grains with homogeneous composition through the bulk. Solar cells made with this material show better performance.

Keywords

Copper Gallium Diselenide, Co-Evaporation, Solar Cell, In-Situ Treatment

1 Introduction

The photovoltaics market is dominated by silicon technologies. However, further cost reductions and efficiency improvements are limited due to Auger recombination [1] and the theoretical maximum efficiency [2]. Developing a tandem structure based on a silicon bottom cell and a wide band gap (~1.7 eV) top cell is of interest to overcome these challenges. $CuIn_{1-x}Ga_xSe_2$ (CIGS) is a top cell material candidate due to its tunable band gap which can be increased by replacing In (x=0) with increasing amounts of Ga ($1 \geq x > 0$). $CuGaSe_2$ (CGS) is of particular interest because it has a well-matched wide band gap of ~1.7 eV [3]. CGS is also indium-free, which is advantageous for industry as indium is a rare element with increasing costs. However, CGS solar cells have limited efficiencies largely due to the formation of $Cu_\delta Se$ phases [4], [5] likely due to kinetic limitations [6]. In addition, it is found that interface recombination caused by low band bending in the bulk limits its efficiency [7]. The activation energy of reaction to form $CuGaSe_2$ is greater than that of $CuInSe_2$, suggesting that it may form at a slower rate [8], [9], [6]. Finally, typical deposition procedures used for CGS were optimized for CIGS and thus do not address this difference.

A modified co-evaporation growth procedure introducing long, high temperature annealing steps to the standard Cu-poor, Cu-rich, Cu-off (CuPRO) procedure was developed by Tsoulka et al. to compensate for the slow kinetics of formation, resulting in larger grains with a more uniform composition and phase distribution [5]. This procedure, CuPRO(M), requires two thirty-minute

"relaxation" steps. This long, high-temperature process is not economical for industrial applications.

In previous work we have shown that metal halides act as transport agents in CIGS and catalyze its crystallization [10], [11], [12], [13], [14], [15]. AgBr has been shown to produce the greatest recrystallization effect in Cu(In,Ga)Se_2 alloys based on these results. Though very little metal halide is used, the cation Ag could introduce known benefits of Ag alloying, even during low-temperature CIGS deposition, including enhanced grain size, crystallinity, and device performance [16], [17]. The Br is anticipated to enhance the rate of atomic transport during growth as shown previously for CIGS films.

Here, AgBr is used to catalyze the recrystallization, grain growth, and phase homogenization of CGS grown by the CuPRO procedure without the long relaxation annealing steps.

2 Experimental Details

2.1 Film and Device Fabrication

CGS films were deposited onto molybdenum-coated soda-lime glass (SLG) substrates by co-evaporation from elemental sources. All depositions were conducted in a Se overpressure and the substrate temperature was held constant at 575°C. Reference samples followed a typical 3-stage CuPRO [18] deposition procedure. During the deposition, Ga and Se were held constant while the Cu flux was adjusted such that the composition transitioned from Cu-poor (Stage 1) to Cu-rich (Stage 2) to Cu-poor (Stage 3). During this final Stage 3 the films are completed to stoichiometry (Cu/Ga~0.95). The other films were deposited based on two modified CuPRO procedures. The first followed the CuPRO(M) procedure [4] which includes two thirty-minute relaxation periods in Se overpressure. These relaxation steps took place (1) after the Cu-rich

Stage 2 and (2) after the Cu-poor Stage 3. The second modified procedure, CuPRO+AgBr, included only the CuPRO process with an evaporation of ~20 mg of AgBr after Stage 2 over a 12-minute period in a Se overpressure. Schematic summaries of the deposition processes are provided in Appendix A.

Some films were used to complete devices with the following architecture: SLG/Mo/CGS/CdS/ZnO/ZnO:Al, where SLG refers to soda-lime glass. After CGS deposition, films were dipped in a 0.05 M KCN solution for two minutes to remove any copper selenide phases from the surface [19]. Chemical bath deposition was used to grow a CdS buffer layer. Details about the optimization of the recipe followed are found in [20] and [21]. A ZnO/ZnO:Al window bi-layer was deposited by rf-sputtering. Ni-Al-Ni metallic grids were deposited using a shadow mask to form 0.5 cm^2 devices which were separated by mechanical scribing.

2.2 Characterization

Film morphologies were studied from scanning electron microscopy (SEM) images taken using a JEOL JSM 7600F at 5 kV acceleration voltage. Time-of-flight secondary ion mass spectroscopy (TOF-SIMS) depth profiling was conducted using an Ion TOF 5 SIMS. A 1 kV Cs^+ ion beam was used for depth profiling and the analysis beam was 30 kV Bi_3. Symmetric θ-2θ X-ray diffraction (XRD) patterns were collected on a D8 Bruker diffractometer with Cu-Kα radiation. Peak parameters were extracted and identified using the International Center for Diffraction Data (ICDD) Database [22].

Device parameters were determined from current density voltage (J-V) data collected under standard testing conditions. The temperature of the metal plate under the sample was held at

25°C by a thermoelectric cooler. The sample was illuminated with an AM1.5 simulated solar spectrum at a power of 1000 W/m^2. External quantum efficiency (EQE) data was collected using a homemade system. Calibrations were conducted from 300 to 980 nm using Si and InGaAs monocrystals, respectively, supplied by Hamamatsu.

3 Results

3.1 Scanning Electron Microscopy

Cross-section and top-view SEM images of the CGS films deposited by the CuPRO, CuPRO(M), and CuPRO+AgBr treatments are shown in Figure 1. The CuPRO film shows a layer of small grains (~0.2 μm diameter) on the molybdenum, indicative of the Cu-poor first stage and larger grains (~0.5 μm) throughout the rest of the film. However, the surface morphology suggests smaller grains ~0.3 μm in diameter. The film deposited by the CuPRO(M) process similarly resulted in a distribution of smaller grains toward the molybdenum and larger grains through the rest of the film. The surface morphology is consistent with grains at least ~0.5 μm in diameter. The CGS film deposited by CuPRO with AgBr treatment resulted in very large, densely packed grains throughout the whole film. It is notable that the grains in the CuPRO+AgBr film appear to span the entire film thickness from the Mo to the surface while the larger grains in the other two samples span only the top half of the film. Despite this, the surface morphology of the CuPRO+AgBr is similar to the other samples.

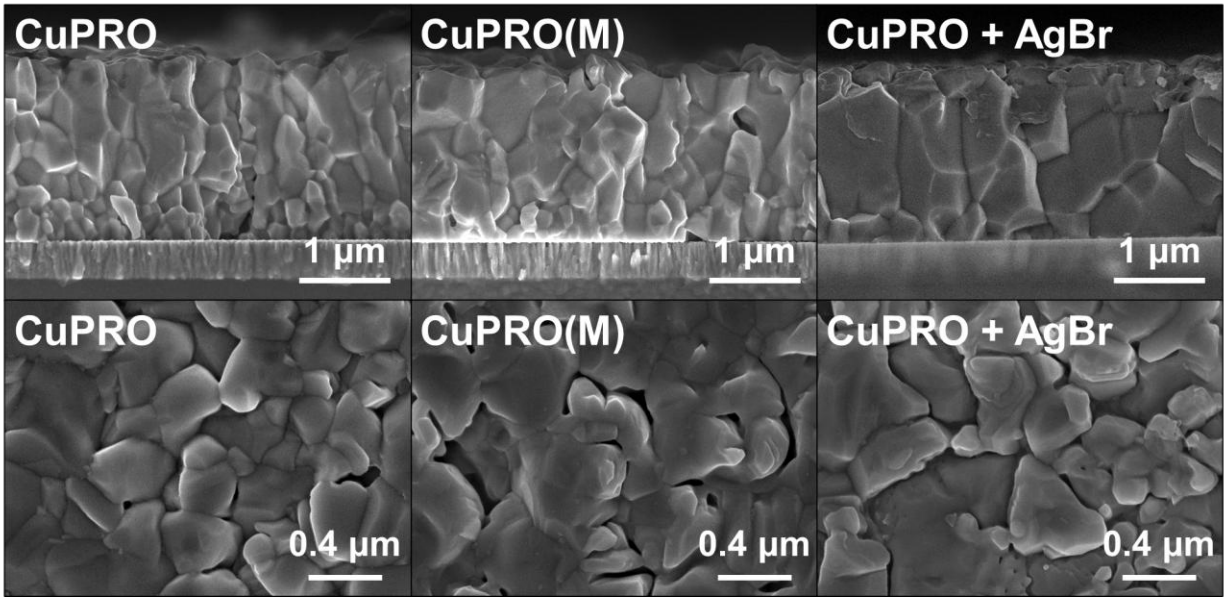

Figure 1: Cross-section and top-view SEM images of CGS films deposited by CuPRO, CuPRO(M), and CuPRO+AgBr processes.

3.2 TOF-SIMS

TOF-SIMS was used to compare the elemental distribution through the CGS films deposited by CuPRO, CuPRO(M), and CuPRO+AgBr (Figure 2). The intensity of each element was normalized to the total ion yield to account for minor drift in the analyzer beam intensity. The Cu, Ga, and Se signals in all samples are mostly constant through the depth of the film, showing the depositions resulted in compositional homogeneity. Ag signal for the film grown with AgBr treatment is shown; the signal is not discernable from background. Trace amounts of Br were detected in the CGS film after the AgBr treatment as determined by a negative ion TOF-SIMS scan (not shown).

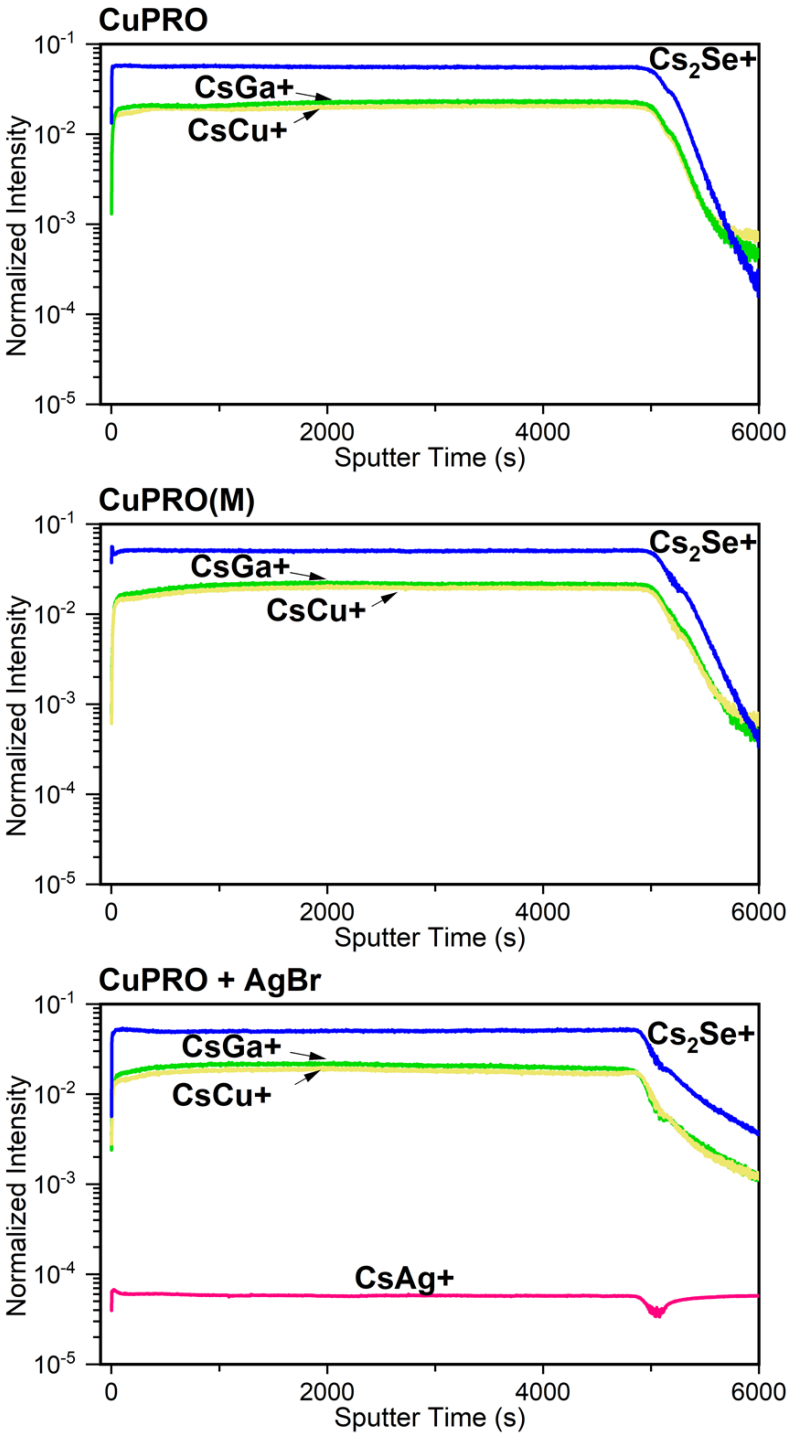

Figure 2: Positive ion TOF-SIMS scans collected for the CuPRO, CuPRO(M), and CuPRO+AgBr samples. The Cu signal is plotted in yellow, the Ga in green, and Se in blue.

3.3 X-Ray Diffraction

Figure 3 shows XRD patterns of the CGS films deposited by CuPRO, CuPRO(M), and CuPRO+AgBr plotted on logarithmic scales. For better interpretation select peaks were measured over smaller 2θ ranges for CuPRO (black), CuPRO(M) (red), and CuPRO+AgBr (blue). Extracted peak characteristics and intensity ratios are summarized in Table I. All patterns have phases identified as chalcopyrite $CuGaSe_2$ (ICDD Ref. 03-065-2735) and Mo (ICDD Ref. 01-089-5156). The characteristic CGS peak positions and full width at half maximum (FWHM) values show little to no differences among the samples. I(112)/I(220+204) varies between samples and I(220)/I(204) is higher for the CuPRO sample. Preferred orientation can change based on the growth recipe used or small variations in composition. The CuPRO sample also shows a secondary phase (2θ ~27.1° and ~44.9°) attributed to a $Cu_{\delta}Se$ phase where δ represents composition and ranges from 1 to 2. This is attributed to a possible Cu-Se segregation within the film which is observed for CGS [4], [5]. The two modified processes, CuPRO(M) and CuPRO+AgBr, both avoid the formation of this secondary phase.

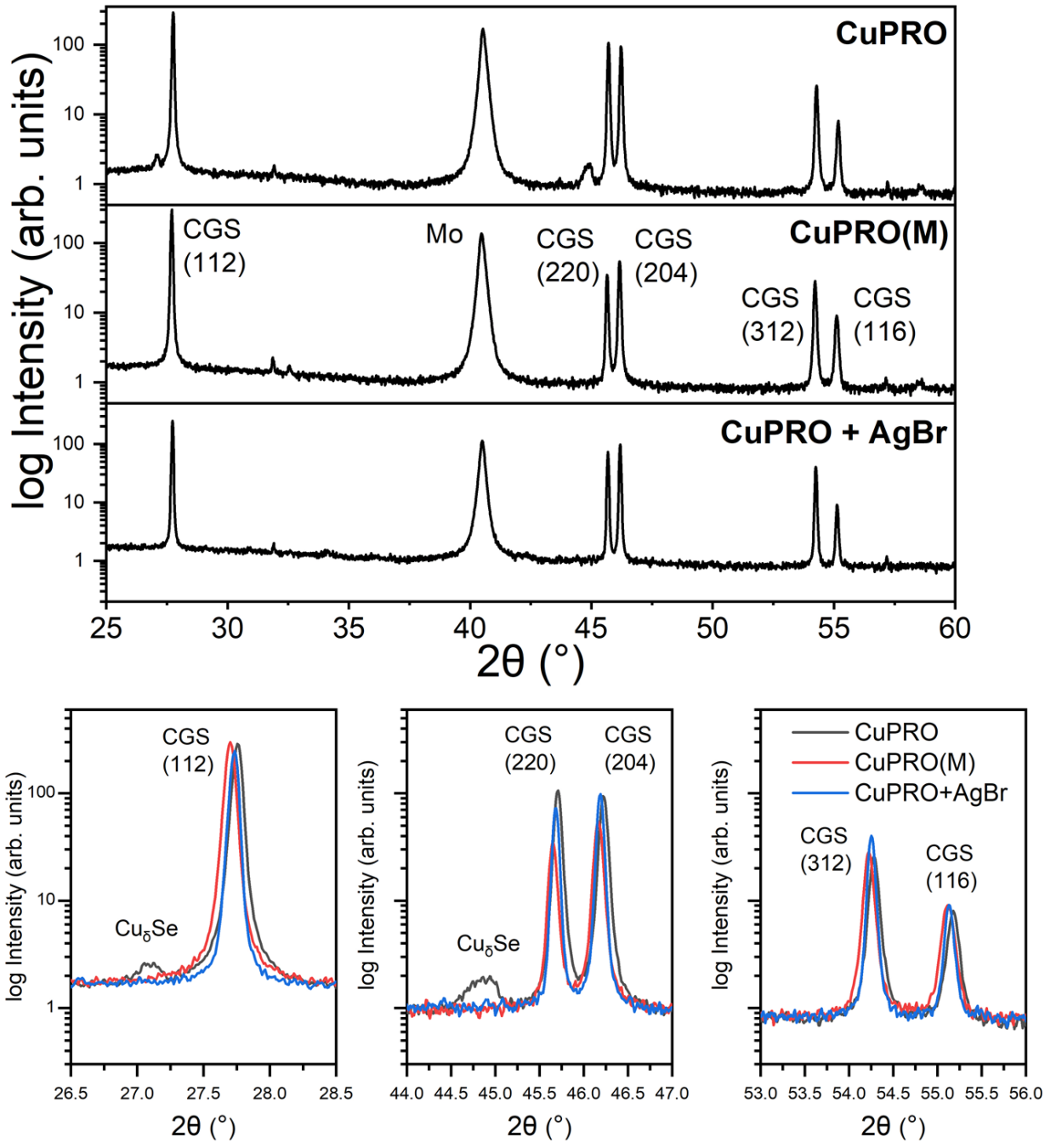

Figure 3: XRD patterns of the CGS films deposited by CuPRO, CuPRO(M), and CuPRO+AgBr treatment. Peaks representing characteristic (112), (220)/(204), and (312)/(116) orientations were plotted over smaller 2θ ranges for interpretation.

Table I: Extracted XRD pattern parameters for CuPRO, CuPRO(M), and CuPRO+AgBr. Intensity ratios were calculated for peaks representing characteristic CGS orientations.

	CuPRO		CuPRO(M)		CuPRO + AgBr	
Characteristic CGS Peak	Position (2θ)	FWHM (°)	Position (2θ)	FWHM (°)	Position (2θ)	FWHM (°)
(112)	27.4	0.07	27.73	0.071	27.74	0.067
(220)	45.67	0.11	45.67	0.11	45.68	0.11
(204)	46.18	0.11	46.18	0.108	46.18	0.106
(312)	54.24	0.14	54.24	0.13	54.25	0.12
(116)	55.13	0.14	55.13	0.14	55.14	0.13
Intensity Ratio	CuPRO		CuPRO(M)		CuPRO + AgBr	
I(112)/I(220+204)	2.29		4.59		3.12	
I(220)/I(204)	1.00		0.61		0.65	
I(312)/I(116)	2.25		2.20		2.67	

3.4 Device Characterization

Devices were fabricated using CGS deposited by CuPRO, CuPRO(M), and CuPRO+AgBr processes. Device parameters are shown in Figure 4 for the five highest efficiency devices made by each deposition procedure. Fill factor (FF) and open-circuit voltage (V_{oc}) were measured by J-V and short-circuit current density (J_{sc}) by EQE per device. Efficiency values were calculated using these values. While there is significant scatter in all of the device parameters, the AgBr treated devices show clear improvement compared to the CuPRO samples and some improvements compared to the CuPRO(M), though the results are within the scatter of the CuPRO(M). In all parameters the AgBr treatment reduced the scatter in the results. Which parameters were responsible for the improvement in the device performance varied with respect to the CuPRO and CuPRO(M) processes. Thus the V_{oc} primarily improved relative to the CuPRO(M) while the J_{sc} primarily improved relative to the CuPRO process, although some of that is accounted for in the short wavelength portion of the spectrum. All FF values are low,

consistent with common observations [23],[4] and the CuPRO(M) values show large amounts of scatter. However, the average FF value improves in the CuPRO+AgBr process relative to both other processes. Finally, there is a relatively clear improvement in the overall efficiency for the CuPRO+AgBr devices relative to the other two processes. Without further detailed analysis it is difficult to estimate the primary limitations to the performance of devices produced by each process. There are too many possible mechanisms to speculate on the mechanism behind the various improvements. Capacitance and temperature based measurements are in progress and results, coupled with device modeling will be reported in a future work.

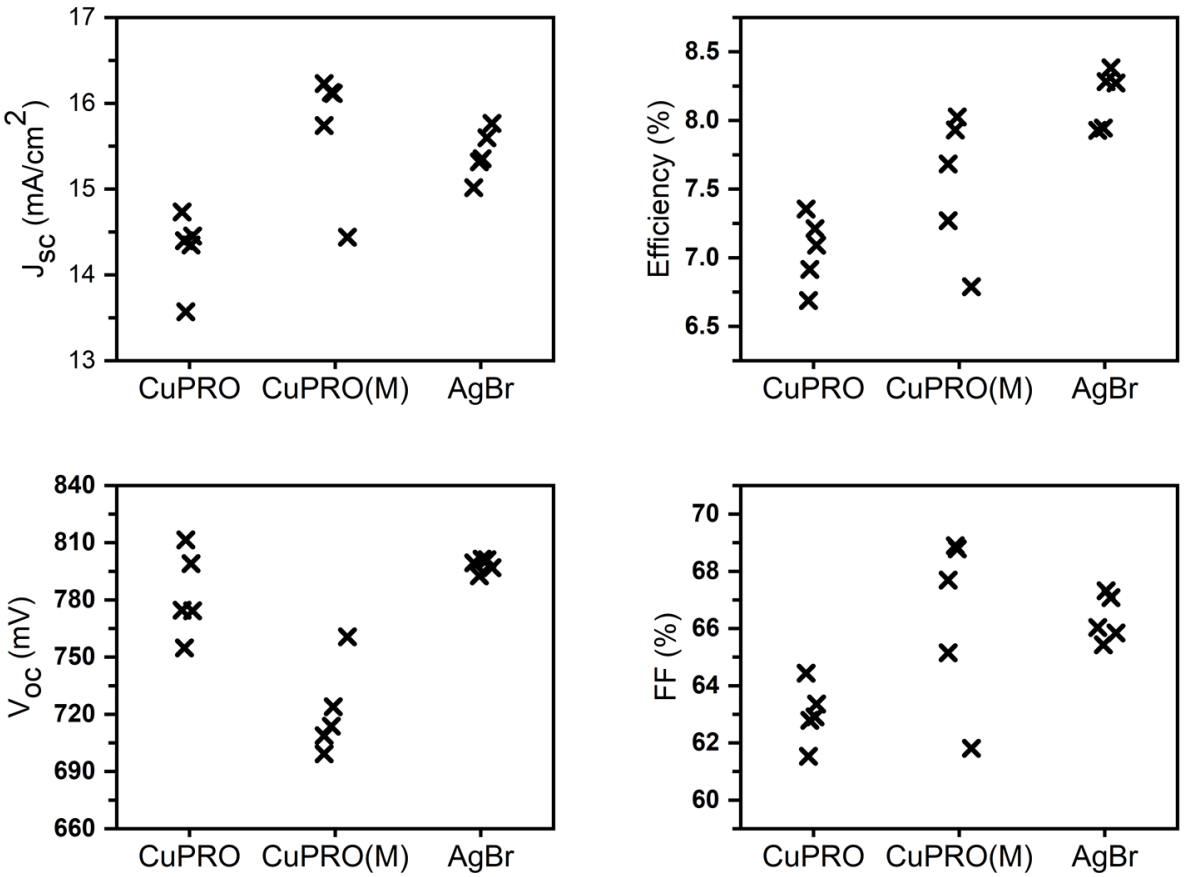

Figure 4: Device parameters for the five highest efficiency (%) devices per deposition procedure. The fill factor (FF) (%) and V_{oc} (mV) were extracted from current density-voltage measurements and J_{sc} (mA/cm^2) values extracted from external quantum efficiency measurements.

EQE measurements were conducted on the CuPRO, CuPRO(M), and CuPRO+AgBr samples and representative curves are shown in Figure 5. The absorption edge of the CuPRO(M) and CuPRO+AgBr samples extend to slightly longer wavelengths and appear to have smaller band gaps compared to the CuPRO. This is likely due to the lack of secondary phases, which have higher band gaps, in the CuPRO(M) and CuPRO+AgBr samples. For CuPRO, the absorption edge has small steps likely due to small variations in composition or phase through the layer and grain to grain. Note that the small differences in the short wavelength region are attributed to differences in the CdS thickness between devices; the same deposition was followed for each device and it appears CdS grows at a different rate on the CuPRO sample. The significance of this is beyond the scope of this work.

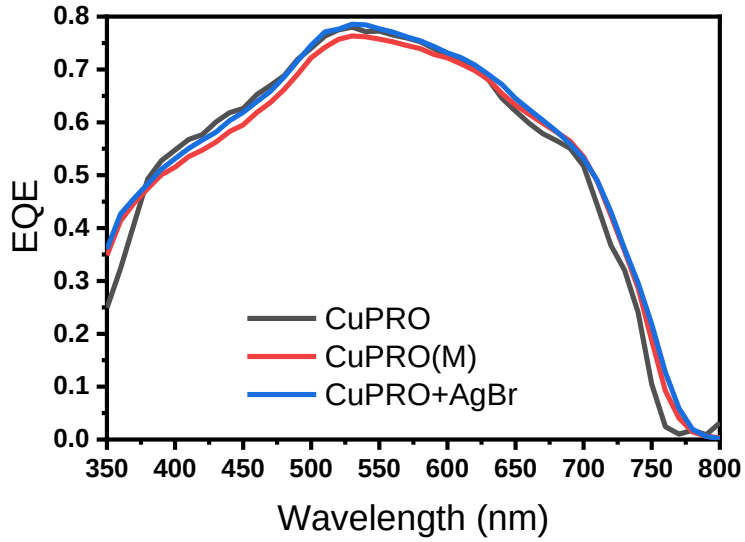

Figure 5: External quantum efficiency (EQE) curves for CGS devices prepared by CuPRO, CuPRO(M), and CuPRO+AgBr.

4 Discussion

Depositing CGS by CuPRO with a AgBr treatment produces structurally and compositionally homogeneous films comparable to those deposited by CuPRO(M). The AgBr treatment reduces total deposition time by approximately 50%, with respect to CuPRO(M), and results in larger grains through the film depth and higher device efficiencies. Note that the devices studied could be further optimized by an anti-reflective coating. Although the elemental distribution was constant through the film depth for all samples (Figure 2), CuPRO+AgBr and CuPRO(M) do not form a Cu-rich phase (Figure 3) as does CuPRO alone. We note that similar $InCl_3$ treatments catalyze amorphous $CuInSe_2$ crystallization and suppress the formation of an intermediate $Cu_{\delta}Se$ phase [15]. This suggests that AgBr is catalyzing the nucleation, growth, and homogenization of the chalcopyrite CGS and possibly suppressing the formation of the $Cu_{\delta}Se$ phase or increasing the rate of its consumption.

We conclude that AgBr works as a transport agent to enhance CGS formation and atomic mobility through the film. After evaporation, the AgBr is expected to dissociate upon adsorbing on the CGS, introducing Br to react with the CGS species. Under the current process conditions, Br would be expected to form volatile intermediate compounds. This could drive increased species transport which is necessary for recrystallization and grain growth. For example, the vapor pressure of $GaBr_3$, a likely intermediate phase, over its own solid is very high (~6.4×10^9 Pa at a substrate temperature of 575°C) [24]. If the $GaBr_3$ can also condense on the grains and

redeposit Ga, this would produce rapid Ga redistribution and hence the observed uniform distribution of Ga through the film. Cu mobility is also enhanced by a similar mechanism but to a lesser extent compared to Ga. The vapor pressure of the expected intermediate phase CuBr at 575°C is approximately $4.5x10^2$ Pa [25]. We note that Cu is also typically a highly mobile species in these compounds so vapor phase transport may be less important.

The introduction of a small amount of Ag by this treatment may also help improve material quality. The introduction of Ag decreases the melting temperature of CIGS [26] which may aid mobility. Ag alloying has also been shown to improve V_{oc}, reduce structural disorder, and possibly decrease defect densities [27]. In the current work, such small amounts of metal halide source are used and so little Ag is detected in the deposited films by SIMS that it is unclear how critical Ag alone is to the improved device performances.

Conclusion

In this work the long "relaxation" steps during CuPRO(M) necessary for the deposition of homogeneous CGS films were replaced by a short AgBr treatment. The AgBr treatment resulted in much larger grains on the scale of the film thickness. Both CuPRO(M) and CuPRO+AgBr showed single phase CGS, demonstrating the removal of a known Cu-rich phase formed during CuPRO deposition. Devices made with CuPRO+AgBr showed V_{oc} improvements and higher efficiencies. Device optimization with an anti-reflective coating and alkali halide post-deposition treatments requires further investigation. Ongoing work is investigating the mechanisms behind device property improvements due to AgBr treatment.

Funding

This material makes use of the TOF-SIMS system at the Colorado School of Mines, which was supported by the National Science Foundation under Grant No.1726898.

This material is based upon work supported by the U.S. Department of Energy's Office of Energy Efficiency and Renewable Energy (EERE) under Solar Energy Technologies Office (SETO) Award Number DE-EE0007551.

References

[1] A. Richter, M. Hermle, and S. Glunz. Reassessment of the limiting efficiency for crystalline silicon solar cells. IEEE Journal of Photovoltaics, 3, 1184-1191, 2013. DOI: 10.1109/JPHOTOV.2013.2270351.

[2] W. Shockley and H. Queisser. Detailed Balance Limit of Efficiency of p-n Junction Solar Cells. Journal of Applied Physics, 32, 510, 1961. DOI: 10.1063/1.1736034.

[3] S. Chichibu, T. Mizutani, K. Murakami, T. Shioda, T. Kurafuji, H. Niki, P.J. Fons, and A. Yamada. Band gap energies of bulk, thin-film, and epitaxial layers of $CuInSe_2$ and $CuGaSe_2$. Journal of Applied Physics, 83, 1998. DOI: https://doi.org/10.1063/1.366588.

[4] P. Tsoulka, A. Rivalland, L. Arzel, and N. Barreau. Improved $CuGaSe_2$ absorber properties through a modified co-evaporation process. Thin Solid Films, 709, 2020. DOI: 10.1016/j.tsf.2020.138224.

[5] P. Tsoulka, N. Barreau, I. Braems, L. Arzel, and S. Harel. Detrimental copper-selenide bulk precipitation in $CuIn_{1-x}Ga_xSe_2$ thin-film solar cells. A possible reason for the limited performance at large x?. Thin Solid Films, 712, 2020. DOI: 10.1016/j.tsf.2020.138297.

[6] W.K. Kim, E.A. Payzant, S. Kim, S.A. Speakman, O.D. Crisalle, and T.J. Anderson. Reaction kinetics of $CuGaSe_2$ formation from a GaSe/CuSe bilayer precursor film. Journal of Crystal Growth, 310, 2987-2994, 2008. DOI: 10.1016/j.jcrysgro.2008.01.034.

[7] J.V. Li, S. Grover, M.A. Contreras, K. Ramanathan, D. Kuciauskas, and R. Noufi. A recombination analysis of $Cu(In,Ga)Se_2$ solar cells with low and high Ga compositions. Solar Energy Materials and Solar Cells, 124, 143-149, 2014. DOI: 10.1016/j.solmat.2014.01.047.

[8] M. Purwins, A. Weber, P. Berwian, G. Müller, F. Hergert, S. Jost, and R. Hock. Kinetics of the reactive crystallization of $CuInSe_2$ and $CuGaSe_2$ chalcopyrite films for solar cell applications. Journal of Crystal Growth, 287, 408-413, 2006. DOI: 10.1016/j.jcrysgro.2005.11.054.

[9] S. Kim, W.K. Kim, R.M. Kaczynski, R.D. Acher, S. Yoon, T.J. Anderson, and O.D. Crisalle. Reaction kinetics of $CuInSe_2$ thin films grown from bilayer InSe/CuSe precursors. Journal of Vacuum Science & Technology A: Vacuum, Surfaces, and Films, 23, 310-315, 2005. DOI: 10.1116/1.1861051.

[10] E. Palmiotti, S. Soltanmohammad, A. Rockett, G. Rajan, S. Karki, B. Belfore, and S. Marsillac. Post-Deposition Recrystallization of Chloride Treated $Cu(In,Ga)\ Se_2$ Thin-Film Solar Cells. 2018 IEEE 7th World Conference on Photovoltaic Energy Conversion (WCPEC) (A Joint Conference of 45th IEEE PVSC, 28th PVSEC & 34th EU PVSEC), 163-166, 2018, DOI: 10.1109/PVSC.2018.8547595.

[11] E. Palmiotti, S. Karki, B. Belfore, S. Soltanmohammad, G. Rajan, S. Marsillac, and A. Rockett. Post-Deposition Recrystallization of Co-Evaporated Cu(In,Ga)Se_2 Films by Bromide Vapor Treatments. 2019 IEEE 46th Photovoltaic Specialists Conference (PVSC), 1863-1866, 2019, DOI: 10.1109/PVSC40753.2019.8980803.

[12] D. Poudel, B. Belfore, T. Ashrafee, E. Palmiotti, S. Karki, G. Rajan, T. Lepetit, A. Rockett, and S. Marsillac. In Situ Recrystallization of Co-Evaporated Cu(In,Ga)Se_2 Thin Films by Copper Chloride Vapor Treatment towards Solar Cell Applications. Energies, 14, 3938, 2021, DOI: 10.3390/en14133938.

[13] D. Poudel, B. Belfore, T. Ashrafee, S. Karki, G. Rajan, A. Rockett, and S. Marsillac. Analysis of Post-Deposition Recrystallization Processing via Indium Bromide of Cu(In,Ga)Se_2 Thin Films. Materials, 14, 3596, DOI: 10.3390/ma14133596.

[14] B. Belfore, D. Poudel, S. Karki, S. Soltanmohammad, E. Palmiotti, T. Lepetit, A. Rockett, and S. Marsillac. Recrystallization of Cu(In,Ga)Se_2 Semiconductor Thin Films via $InCl_3$ Treatment. Thin Solid Films, 735, 2021.

[15] E. Palmiotti, B. Belfore, D. Poudel, S. Marsillac, A. Rockett. In-Situ Study of the Crystallization of Amorphous $CuInSe_2$ Thin Films and the Effect of $InCl_3$ Treatment. Thin Solid Films, 746, 2022, DOI: https://doi.org/10.1016/j.tsf.2022.139095.

[16] [4] K. Kim, J. Park, J. Yoo, J. Cho, H. Lee, and J. Yun, “Ag incorporation in low-temperature grown Cu(In,Ga)Se2 solar cells using Ag precursor layers”, Solar Energy Materials & Solar Cells, 146, 114-120, 2016. DOI: 10.1016/j.solmat.2015.11.028.

[17] L. Chen, J. Lee, and W. Shafarman, “The Comparison of (Ag,Cu)(In,Ga)Se2 and Cu(In,Ga)Se2 Thin Films Deposited by Three-Stage Coevaporation”, IEEE Journal of Photovoltaics, 4, 1, 2014.

[18] J. Kessler, C. Chityuttakan, J. Lu, J. Schöldström, and L. Stolt. Cu(In,Ga)Se_2 Thin Films Grown with a Cu-Poor/Rich/Poor Sequence: Growth Model and Structural Considerations. Progress in Photovoltaics: Research and Applications, 11, 319-331, 2003. DOI: 10.1002/pip.495.

[19] J. Lehmann, S. Lehmann, I. Lauermann, T. Rissom, C.A. Kaufmann, M.C. Lux-Steiner, M. Bär, S. Sadewasser. Reliable wet-chemical cleaning of natively oxidized high-efficiency Cu(In,Ga)Se_2 thin-film solar cell absorbers, J. Appl. Phys., 116, 2014. DOI: 10.1063/1.4903976.

[20] L. Choubrac, G. Brammertz, N. Barreau, L. Arzel, S. Harel, M. Meuris, and B. Vermang. 7.6% CZGSe Solar Cells Thanks to Optimized CdS Chemical Bath Deposition. Physica Status Solidi (A) Applications and Materials Science, 215, 1-9, 2018. DOI: 10.1002/pssa.201800043.

[21] T. Kodalle, Léo Choubrac, L. Arzel, R. Schlatmann, N. Barreau, and C. A. Kaufmann. Effects of KF and RbF post deposition treatments on the growth of the CdS buffer layer on CIGS thin films – a comparative study. Solar Energy Materials and Solar Cells, 200, 2019. DOI: 10.1016/j.solmat.2019.109997.

[22] S. Gates-Rector and T. Blanton. The Powder Diffraction File: A Quality Materials Characterization Database. Powder Diffr., (2019).

[23] S. Ishizuka, A. Yamada, P. Fons, H. Shibata, and S. Niki. Structural tuning of wide-gap chalcopyrite $CuGaSe_2$ thin films and highly efficient solar cells: differences from narrow-gap Cu(In,Ga)Se_2. Progress in Photovoltaics, 22, 2014. DOI: 10.1002/pip.

[24] B. Brunetti, V. Piacente, and P. Scardala. A Study on the Sublimation of Gallium Tribromide. Journal of Chemical and Engineering Data, 54, 2273-2276, 2009.

[25] A. Iizuka, E. Shibata, M. Sato, N. Onodera, and T. Nakamura. Vapor pressure measurements of CuBr and $ZnBr_2$ by the Knudsen effusion method and their vapor species identification. Thermochimica Acta, 593, 1-6, 2014. DOI: 10.1016/j.tca.2014.08.003.

[26] J.L. Shay and J.H. Wernick. Ternary Chalcopyrite Semiconductors: Growth, Electronic Properties, and Applications. Pergamon Press, 1975.

[27] P.T. Erslev, J. Lee, G.M. Hanket, W.N. Shafarman, and J.D. Cohen. The electronic structure of $Cu(In_{1-x}Ga_x)Se_2$ alloyed with silver. Thin Solid Films, 519, 7296-7299, 2011. DOI: 10.1016/j.tsf.2011.01.368.

Appendix A

Figure Appendix 1 shows qualitative schematics of the deposition fluxes in the procedures followed. Cu transitions were monitored by end-point-detection using the output power of the substrate temperature controller as described in [18].

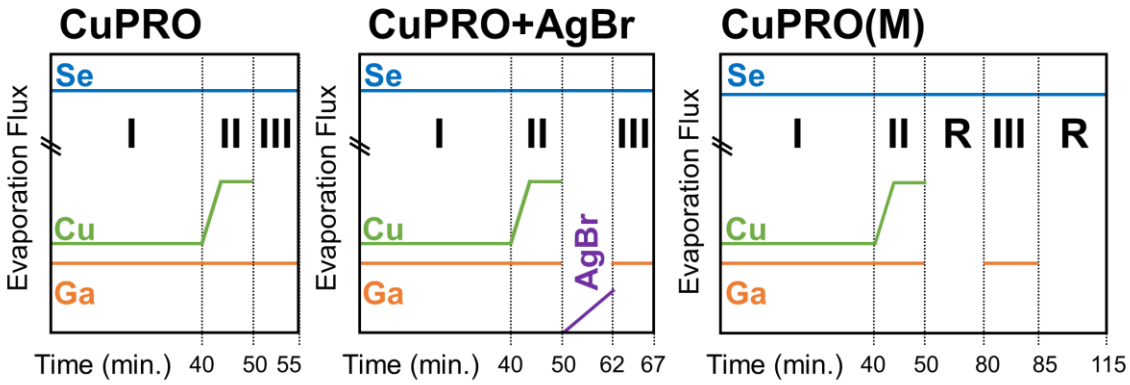

Figure Appendix 1: Schematics of the deposition recipes followed to deposit CGS films by CuPRO, CuPRO+AgBr, and CUPRO(M). Note that the evaporation fluxes are relative and times are approximate. The stages are respectively labeled as I, II, and III. The “relaxation” steps in CuPRO(M) are labeled as R.